Bayesian inference of force dynamics during morphogenesis

Shuji Ishihara [a,*], Kaoru Sugimura [b,c,**]

[a] Graduate School of Arts and Sciences, The University of Tokyo, Tokyo 153-8902, Japan
[b] Institute for Integrated Cell-Material Sciences (WPI-iCeMS), Kyoto University, Kyoto 606-8501, Japan
[c] RIKEN Brain Science Institute, Saitama 351-0198, Japan

HIGHLIGHTS

► A novel method to estimate the cell pressure and the cortical tension is developed.
► The inverse problem is formulated based on Bayesian statistics.
► The described method is proven to provide a reasonable estimate of forces *in vivo*.

GRAPHICAL ABSTRACT
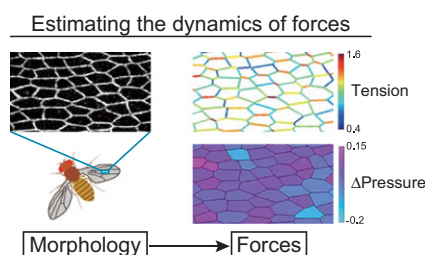
ABSTRACT

During morphogenesis, cells push and pull each other to trigger precise deformations of a tissue to shape the body. Therefore, to understand the development of animal forms, it is essential to analyze how mechanical forces coordinate behaviors of individual cells that underlie tissue deformations. However, the lack of a direct and non-invasive force-measurement method has hampered our ability to identify the underlying physical principles required to regulate morphogenesis. In this study, by employing Bayesian statistics, we develop a novel inverse problem framework to estimate the pressure of each cell and the tension of each contact surface from the observed geometry of the cells. We confirmed that the true and estimated values of forces fit well in artificially generated data sets. Moreover, estimates of forces in *Drosophila* epithelial tissues are consistent with other readouts of forces obtained by indirect or invasive methods such as laser-induced destruction of cortical actin cables. Using the method, we clarify the developmental changes in the patterns of tensile force in the *Drosophila* dorsal thorax. In summary, the batch and noninvasive nature of the described force-estimation method will enable us to analyze the mechanical control of morphogenesis at an unprecedented quantitative level.

1. Introduction

In the course of animal development, tissues undergo a series of deformations. These processes are realized by the coordination of the spatio-temporal profiles of the activity of proteins and the mechanical force that acts directly on cell shape (Bilder and Haigo, 2012; Eaton and Julicher, 2012; Kasza and Zallen, 2011; Lecuit et al., 2011; Nahmad and Lander, 2011; Wartlick and Gonzalez-Gaitan, 2011). Therefore, to understand fully the regulation of development, it is essential to clarify how this mechanical force that drives tissue deformation emerges from the molecular properties of the constituent cells and how a generated pattern of a stress field regulates the correct patterning of a tissue.

In epithelial tissue, the morphogenetic process is driven by how cells push and pull each other along the plane of the

adherens junction by generating forces, i.e., tension that shortens a contact surface (cell–cell surface) and pressure that counteracts the tension to maintain the size of a cell (Fig. 1A) (Lecuit and Lenne, 2007; Mofrad and Kamm, 2006). The active generation of tension by myosin is amenable to genetic and pharmacological

Fig. 1. Outline of the force-estimation method. (A) The structure and forces in an epithelial sheet. (1) Cortical actin cables (red) run along the plane of the adherens junctions. (2) Tension shortens an edge. Pressure maintains the size of a cell. (B) Procedure for estimating forces. (1) Input: an image of the cells (*Drosophila* wing at 23 h after puparium formation (APF)). (2) Assign unknown variables: the tension of each edge and the pressure of each cell. Consider the balance of forces at each vertex. (3) Output: the distribution of tension (left) and relative pressure (right; the difference in the pressure among cells is shown). (C) An inverse problem framework. (1) The number of indefiniteness is $R+1+f$ with R surrounding cells and "f 4-way junctions". (2) Bayes's theorem $P(\mathbf{p}|\mathbf{b}) \propto P(\mathbf{b}|\mathbf{p})\,\pi_T(\mathbf{p})$ gives the posterior distribution $P(\mathbf{p}|\mathbf{b})$, by which unknown values of $\mathbf{p}$ (P_i and T_{ij}) are estimated. Our expectation that tensions are distributed around a positive value T_c is introduced by $\pi_T(\mathbf{p})$, which obeys Gaussian distribution with mean T_c and variance ω^2. μ, the weight of the second term (regularization term) in Eq. (7), is determined from ratio between variances of the likelihood and of prior functions (σ^2 and ω^2; see Eq. (4) and (5)). (D) The stress field acting on a group of cells can be estimated using the equations shown. The longest axis of a stress ellipse is the maximum stress direction along which forces work most strongly in a cell population. Scale bar: 10 μm (B1). (For interpretation of the references to color in this figure legend, the reader is referred to the web version of this article.)

manipulation and can be probed locally by laser-induced destruction of the cortical actin cables, where the vertices of an irradiated edge moving apart indicates positive tension contracting the edge, and a larger velocity of the vertices represents higher tension (Hutson et al., 2003; Rauzi et al., 2008). These approaches have elucidated how changes in the geometry of cells are determined by the activity and/or localization of force-generating molecular machinery within a cell (Kasza and Zallen, 2011; Lecuit et al., 2011; Mason and Martin, 2011; Paluch and Heisenberg., 2009). On the other hand, an analysis of how the macroscopic stress controls the precise deformation of the developing tissue has been limited by the lack of proper experimental methods to evaluate the global distribution of the tensions and the pressures; laser cutting is an invasive method that measures the tension of a single edge, and previous approaches such as Particle Image Velocimetry (PIV), which characterizes the deformation of cells, do not measure pressure or tension (Paluch and Heisenberg., 2009; Raffel et al., 1998; Supatto et al., 2005). Therefore, a comprehensive analysis of how morphogenetic cellular behaviors are regulated by the global balance of stress within a cell population/tissue awaits a global readout of the dynamics of the forces.

The present study aims to provide a new way to quantify the global distribution of forces inside a living animal. By considering the balance among tensions of contact surfaces and pressures of individual cells, one can estimate the values of these forces from the observed geometry of the cells. However, it transpires that the problem has inherent indefiniteness that does not allow us to determine the unique solution. To handle the indefiniteness, the force balance and our expectation of the system are integrated by adopting Bayesian statistics, which enables us to obtain the most plausible estimation by adjusting the balance between fit-of-data and our expectation of the system. This feature of our method represents an advantage over other methods (Brodland et al., 2010; Chiou et al., 2012; see details in Discussion). We confirmed that the true and estimated values of forces fit an artificially generated data set very well. Furthermore, to validate our method *in vivo*, we compared the estimated values with results obtained by other indirect or invasive methods such as laser ablation of a contact surface. Our results strongly suggest that the described method provides a reasonable estimate of forces in a developing tissue. Finally, we applied our method to the *Drosophila* epithelial tissues and examined developmental changes in the stress field.
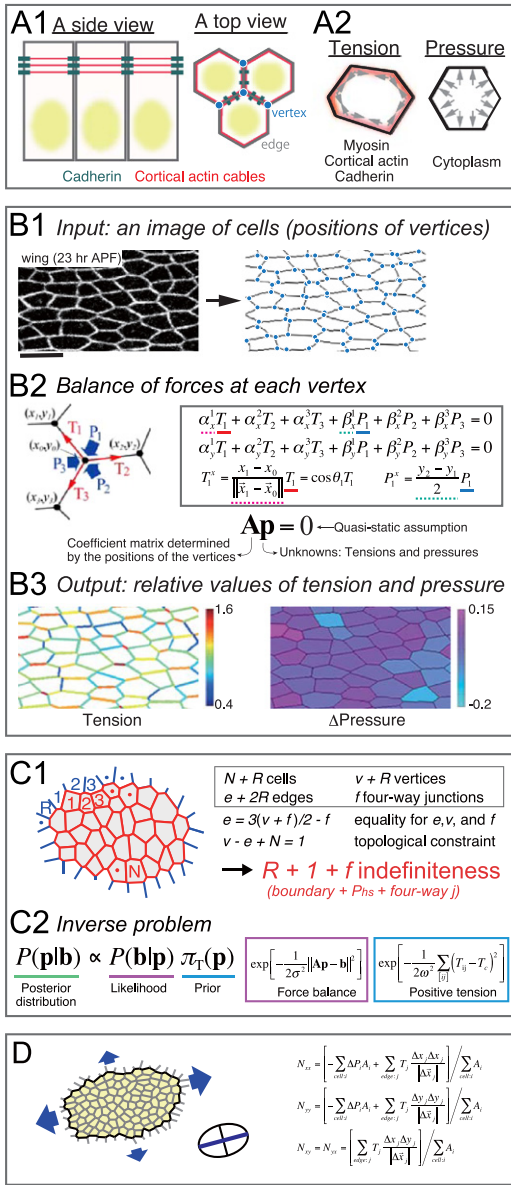
2. Results

2.1. Force-estimation method

2.1.1. Balance equation of forces

We approximated an epithelial tissue as a 2-dimensoinal sheet (Aigouy et al., 2011; Bosveld et al., 2012; Farhadifar et al., 2007; Honda, 1983; Rauzi et al., 2008). To estimate tensions and pressures (Fig. 1A2), let us consider balance of forces represented by tensile forces of individual contact surface and cell pressures. In a cell population approximated by polygons (Fig. 1B1), with assignment of the unknown variables T_{ij} (tension of each contact surface) and P_i (pressure of each cell), the forces at the 0th vertex in Fig. 1B2, $\mathbf{f}_0=(f_0^x, f_0^y)$, are given as follows:

$$f_0^x = \alpha_1^x T_1 + \alpha_2^x T_2 + \alpha_3^x T_3 + \beta_1^x P_1 + \beta_2^x P_2 + \beta_3^x P_3$$

$$f_0^y = \alpha_1^y T_1 + \alpha_2^y T_2 + \alpha_3^y T_3 + \beta_1^y P_1 + \beta_2^y P_2 + \beta_3^y P_3 \qquad (1)$$

Coefficients α and β are obtained by considering virtual displacement of the 0th vertex and thus they are determined

only from the relative positions of the vertices as follows. Coefficients of tensions simply depend on the angle of the edge; $\alpha_1^x = (x_1 - x_0)/||\mathbf{x}_1 - \mathbf{x}_0|| = \cos\theta_1$, $\alpha_1^y = (y_1 - y_0)/||\mathbf{x}_1 - \mathbf{x}_0|| = \sin\theta_1$, etc. Coefficients of pressures are given as $\beta_1^x = (y_2 - y_1)/2$, $\beta_1^y = -(x_2 - x_1)/2$, etc. While Eq. (1) is valid for any forms of tensions and pressures, the derivation becomes clearer when we assume a potential function for the forces as explained below. Let us consider a single cell that is approximated by a 2-dimensional n-sided polygon characterized by its vertices positioned at $\mathbf{x}_0$, $\mathbf{x}_1,\dots,\mathbf{x}_{n-1}$ in counter-clockwise order. With $\mathbf{x}_n = \mathbf{x}_0$, the area of the cell is provided by $A = (1/2)\sum_{i=0}^{n-1} \mathbf{x}_i \times \mathbf{x}_{i+1}$, and the lengths of edges are given by $l_i = ||\mathbf{x}_{i+1} - \mathbf{x}_i||$ ($i = 0, 1, \dots, n-1$). In general, the potential energy of the cell depends on the area and the lengths of edges, i.e., $U = U(l_0, l_1, \dots, l_{n-1}, A)$, therefore the force on the ith vertex, $f_i = (f_i^x, f_i^y)$, is given by the partial differentiation of the potential energy with respect to $\mathbf{x}_i$, i.e., $f_i = -\partial U/\partial \mathbf{x}_i = -(\partial U/\partial l_{i-1})(\partial l_{i-1}/\partial \mathbf{x}_i) - (\partial U/\partial l_i)(\partial l_i/\partial \mathbf{x}_i) - (\partial U/\partial A)(\partial A/\partial \mathbf{x}_i)$. Since the pressure of the cell and the tensions of edges are defined as $T_i = \partial U/\partial l_i$ and $P = -\partial U/\partial A$, respectively, $\mathbf{f}_i$ is given in terms of the pressure and tensions as follows.

$$f_i^x = \frac{x_{i-1} - x_i}{l_{i-1}} T_{i-1} + \frac{x_{i+1} - x_i}{l_i} T_i + \frac{y_{i+1} - y_{i-1}}{2} P$$
$$f_i^y = \frac{y_{i-1} - y_i}{l_{i-1}} T_{i-1} + \frac{y_{i+1} - y_i}{l_i} T_i + \frac{x_{i-1} - x_{i+1}}{2} P \qquad (2)$$

This argument validates force balance equation given in Eq. (1). Note that the pressure that applies to the whole line between two neighboring vertices is derived by these arguments and thus dose not give independent force balance condition.

Repeating the derivation of force balance equations for every vertex, a unified vector of forces $\mathbf{F} = (f_0^x, f_0^y, f_1^x, f_1^y, \dots)$ is expressed as $\mathbf{F} = \mathbf{Ap}$, where A is an $n \times m$ matrix composed of coefficients α and β, and $\mathbf{p} = (\mathbf{T}, \mathbf{P})$ is an m-dimensional vector composed of T_{ij} and P_i. n is the number of components in the vector $\mathbf{F}$, and m is that of unknown variables. Since it was suggested that relaxation by viscous dissipation occurs at much shorter time scales (~ 1 min) than morphogenetic processes (minutes to hours) (Moore et al., 1995), the shape of each cell would nearly maintain its statically balanced configuration during its movement (quasi-static assumption); hence, the balance of forces is expressed as

$$\mathbf{Ap} = 0 \qquad (3)$$

This equation allows us to estimate pressure and tension from a snapshot of cells (Fig. 1B3; but see below for indefiniteness in the problem).

2.1.2. The number of indefiniteness in the problem

Consider data comprising N cells, the surrounding R cells, $v + R$ vertices, and $e + 2R$ edges (Fig. 1C1; note that addition of one surrounding cell increases one vertex and two edges, which determines coefficients of R). If all junctions are 3-way, $e = 3v/2$ is satisfied. Using Euler's theorem, $v - e + N = 1$ (Henle, 1994), we can show that the numbers of edges and vertices are given by $e = 3N + 2R - 3$ and $v = 2N + R - 2$, respectively. Here, the number of unknown variables is that of the cells and edges ($4N + 3R - 3$) and the number of conditions is twice that of the vertices ($4N + 2R - 4$). Thus, there exists $R + 1$ indefiniteness. If the data contain f 4-way junctions, the relationship between e and v becomes $e = 3(v + f)/2 - f$. Consequently, indefiniteness equals $R + 1 + f$, indicating that each 4-way junction introduces one indefiniteness. Collectively, in matrix A in the force balance equation, n is smaller than m by $R + 1 + f$.

The above argument clearly indicates that it is difficult to estimate forces in an epithelial sheet because of the inherent shortage of conditions to determine the unknown variables in the force balance equation. Hence, it is critical to define the physical origins of indefiniteness in order to ensure correct interpretation

of the force-estimation data. One indefiniteness arises from the hydrostatic pressure (P_{hs}), since a uniform increase of P_i does not change the balance of force thus shapes of cells. The other R indefiniteness arises from unsolved boundary conditions. In our estimation, we ignored the component of hydrostatic pressure and estimated the differences in pressure among individual cells. Accordingly, we obtained relative values for the forces: $p_i = cP_i - P_{hs}$ and $t_{ij} = cT_{ij}$, where c is a constant (Fig. 1B3). We handle the indefiniteness arisen from boundary condition by Bayesian formulation as explained in the next section.

2.1.3. Inverse problem

To handle the indefiniteness in force balance equation $\mathbf{Ap} = 0$, we adopted the framework of Bayesian statistics as follows (Fig. 1C2) (Akaike, 1980; Kaipio and Somersalo, 2004). Here $\mathbf{A}$ is $n \times m$ matrix in which n and m are the numbers of conditions and unknown variables, respectively. Because n is smaller than m, $\mathbf{p}$ should be solved by introducing plausible assumptions. We expect that the cortical tensions should be positive as verified by laser cutting experiments (Hutson et al., 2003; Rauzi et al., 2008), and thus tensions are distributed around a constant value $T_c > 0$ as

$$\pi_T(\mathbf{p}; \omega^2) = \frac{1}{(2\pi\omega^2)^{m'/2}} \exp\left[-\frac{1}{2\omega^2} \sum_{[ij]} (T_{ij} - T_c)^2\right], \qquad (4)$$

where T_{ij} represents tension of the contact surface between ith and jth cells, and summation is conducted over all of the edges denoted by $[ij]$. m' is the number of edges. T_c can be set $= 1$ due to the arbitrary scale of force in our estimation method. $\pi_T(\mathbf{p})$ represents Gaussian distribution with variance ω^2 that is determined from data as explained later see Eq. (9), and gives the prior function for tensions. We also introduce Dirac's delta function $\delta(\mathbf{p} \cdot \mathbf{p}_{hs})$ as a prior function for pressures to ignore the hydrostatic effect; $\mathbf{p} \cdot \mathbf{p}_{hs}$ is an inner product between vectors $\mathbf{p}$ and $\mathbf{p}_{hs}$, in which $\mathbf{p}_{hs}$ is a zero eigenvector of $\mathbf{A}$ (i.e., $\mathbf{Ap}_{hs} = 0$) corresponding to the indefinite hydrostatic pressure with component $P_i = 1$ and $T_{ij} = 0$ for all i and $[ij]$, respectively. $\pi_T(\mathbf{p}) \times \delta(\mathbf{p} \cdot \mathbf{p}_{hs})$ gives the prior function for our method.

Next, we consider the balance equation Eq. (3) that is determined from observed data. For the sake of clarity, let us generalize the equation as $\mathbf{Ap} = \mathbf{b}$, where $\mathbf{b}$ is an observable quantity ($\mathbf{b} = 0$ in our case). The equations should not be exactly correct, due to unavoidable observation and system errors, where the errors are assumed to obey a Gaussian distribution with variance σ^2. Then the probability to observe $\mathbf{b}$ under given p is written as

$$P(\mathbf{b}|\mathbf{p}; \sigma^2) = \frac{1}{(2\pi\sigma^2)^{n/2}} \exp\left[-\frac{1}{2\sigma^2} \|\mathbf{Ap} - \mathbf{b}\|^2\right] \qquad (5)$$

This gives a likelihood function. Then, according to Bayes's theorem, unknown values of $\mathbf{p}$ (P_i and T_{ij}) are estimated by the posterior distribution $P(\mathbf{p}|\mathbf{b})$.

$$P(\mathbf{p}|\mathbf{b}) \propto P(\mathbf{b}|\mathbf{p})\pi_T(\mathbf{p})\delta(\mathbf{p} \cdot \mathbf{p}_{hs}) \qquad (6)$$

The most probable estimation for $\mathbf{p}$ is obtained at the maximum values of the posterior distribution. Let us define a function $F(\mathbf{p})$ as

$$F(\mathbf{p}) = \|\mathbf{Ap} - \mathbf{b}\|^2 + \mu\|\mathbf{Bp} - \mathbf{g}\|^2 \qquad (7)$$

with $\mu = \sigma^2/\omega^2$, where $\Sigma_{[ij]} (T_{ij} - T_c)^2$ in Eq. (4) is expressed as $||\mathbf{Bp} - \mathbf{g}||^2$. Note that μ, the weight of the second term, is determined from ratio between variances of the likelihood and prior functions (σ^2 and ω^2; see Eqs. (4) and (5)). Then $P(\mathbf{p}|\mathbf{b})$ is written as $P(\mathbf{p}|\mathbf{b}) \propto \exp[-F(\mathbf{p})/2\sigma^2]\delta(\mathbf{p} \cdot \mathbf{p}_{hs})$, indicating that estimation of $\mathbf{p}$ is given by minimizing the function $F(\mathbf{p})$ under the constraint that $\mathbf{p}$ is perpendicular to $\mathbf{p}_{hs}$.

Hyper-parameters σ^2 and ω^2 (thus μ) are determined by minimizing Kullback–Leibler distance between a posterior distribution Eq. (6) and empirical distribution (Akaike, 1980). This is equivalent to maximizing the marginal likelihood function $L(\sigma^2, \mu)$, or minimizing Akaike's Bayesian information criterion (ABIC),

$$L(\sigma^2,\mu) = \int P(\mathbf{b}|\mathbf{p})\pi_T(\mathbf{p})\delta(\mathbf{p} \cdot \mathbf{p}_{hs})d\mathbf{p} \tag{8}$$

The value at which $L(\sigma^2, \mu)$ becomes maximum provides estimations for σ^2 and μ (Kaipio and Somersalo, 2004). By integrating Eq. (8) with respect to $\mathbf{p}$, $L(\sigma^2, \mu)$ is given by the following equation:

$$\max_{\sigma^2,\mu} L(\sigma^2,\mu) = \max_{\mu} \left(\frac{2\pi e E_\mu}{n-m_0+1} \right)^{-\frac{n-m_0+1}{2}} \frac{\underline{\det}\left[\mu \mathbf{B}^\mathbf{T}\mathbf{B} \right]^{1/2}}{\underline{\det}\left[\mathbf{A}^\mathbf{T}\mathbf{A}+\mu \mathbf{B}^\mathbf{T}\mathbf{B} \right]^{1/2}} \tag{9}$$

Here, E_μ is the minimum value of $F(\mathbf{p})$ at a given μ, m_0 is the number of zero eigenvalues of $\mathbf{B}^\mathbf{T}\mathbf{B}$, and $\underline{\det}[\mathbf{M}]$ indicates the product of all non-zero eigenvalues of matrix $\mathbf{M}$.

2.1.4. Implementation of numerical maximization step

To numerically maximize marginal likelihood $L(\sigma^2,\mu)$ with respect to μ, the following procedure is employed (Demmel, 1997). With fixed value of $\mu=\tau^2$, consider the following $(n+m) \times (m+1)$ matrix $\mathbf{S}$;

$$\mathbf{S} = \begin{pmatrix} \mathbf{A} & \mathbf{b} \\ \tau\mathbf{B} & \mathbf{g} \end{pmatrix} \tag{10}$$

QR decomposition of $\mathbf{S}$ is given as $\mathbf{S}=\mathbf{QR}$ where $\mathbf{Q}$ and $\mathbf{R}$ are $(n+m) \times (n+m)$ orthogonal and $(n+m) \times (m+1)$ upper triangular matrix, respectively. Upper $(m+1) \times (m+1)$ square part of $\mathbf{R}$ is expressed as

$$\mathbf{R} = \begin{pmatrix} \mathbf{H} & \mathbf{h} \\ \mathbf{0}^T & h \end{pmatrix}, \tag{11}$$

where $\mathbf{H}$ is $m \times m$ triangular matrix. $\mathbf{H}$ has one zero diagonal component due to the indefiniteness for hydrostatic pressure; $[\mathbf{H}]_{mm}=0$. Then, $F(\mathbf{p})$ in Eq. (7) is written as

$$\|\mathbf{Ap}-\mathbf{b}\|^2 + \mu\|\mathbf{Bp}-\mathbf{g}\|^2 = \|\mathbf{Hp}-\mathbf{h}\|^2 + h^2 \tag{12}$$

This indicates that $\mathbf{p}$ can be evaluated by the condition $||\mathbf{Hp}-\mathbf{h}||^2=0$, at which E_μ is evaluated as $E_\mu=h^2$. In addition, $\underline{\det}[\mathbf{A}^\mathbf{T}\mathbf{A}+\mu\mathbf{B}^\mathbf{T}\mathbf{B}]$ is given by the product of non-zero diagonal components of $[\mathbf{H}]_{ii}$ ($i=1,\dots, m-1$). Therefore, it is possible to evaluate the marginal likelihood $L(\sigma^2,\mu)$ without solving $\mathbf{p}$, which considerably reduces computational steps necessary for the maximizing process.

After the maximization is finished to determine the value of μ, $\mathbf{p}$ is evaluated by calculating

$$\mathbf{p} = \mathbf{H}^{-1}\mathbf{h}, \tag{13}$$

where $\mathbf{H}^{-1}$ is the Moore–Penrose pseudo inverse matrix of $\mathbf{H}$. Since $\mathbf{H}^{-1}$ eliminates the component parallel to $\mathbf{p}_{hs}$, this solution autonomously satisfies the condition to be perpendicular to $\mathbf{p}_{hs}$.

2.1.5. Stress tensor for larger scale mechanics

Once the pressure of each cell and the tension of each edge are estimated, they can be integrated to evaluate the stress tensor $\mathbf{N}$ at a larger scale (group of cells) (Fig. 1D) by the following expression (Batchelor, 1970):

$$N_{\mu v} = \left[-\sum_{i:\text{cell}} P_i A_i \delta_{\mu v} + \sum_{[ij]:\text{edge}} T_{ij} \frac{l_{ij}^\mu l_{ij}^v}{\|\mathbf{l}_{ij}\|} \right] \Big/ \sum_{i:\text{cell}} A_i \tag{14}$$

Here, (μ,v) are indices for (x,y) and $\delta_{\mu v}$ is Kronecker's delta. A_i is the area of the ith cell in the plane of the adherens junction, and $\mathbf{l}_{ij}=(l_{ij}{}^x, l_{ij}{}^y)$ is a vector representation of the edge shared by the ith and jth cell. A stress ellipse is a useful expression of $\mathbf{N}$ (an ellipse in Fig. 1D). The integrated tension determines the maximum stress direction of a tissue along which forces work most strongly in a cell population (the longest axis of a stress ellipse). Since the hydrostatic pressure is unavailable in our method, we evaluated $\mathbf{N}_{\mu v}$ by substituting ΔP_i to P_i in the above equation. The maximum stress direction is independent of the indefiniteness of hydrostatic pressure. The local stress tensor is calculated for individual cells which is defined by $N^i_{\mu v}=(-\Delta P_i \ A_i+\Sigma_{[ij]} \ T_{ij} \ l_{ij}^\mu \ l_{ij}{}^v/\|\mathbf{l}_{ij}\|)/A_i$ (i: index of cell, μ, v: x or y, $\Sigma_{[ij]}$: summation on the contact surfaces between the ith and adjacent cells).

2.2. Validation using artificially generated data set

To evaluate the accuracy of the force-estimation method, we performed a test using artificially generated data (Fig. 2). To obtain artificial data, we performed numerical simulations of a vertex cell model in which potential energy is relaxed with respect to the positions of the vertices $\{\mathbf{x}_i\}$ under free boundary conditions (Fig. 2A) (Farhadifar et al., 2007; Honda, 1983; Käfer et al., 2007; Lecuit and Lenne, 2007; Mofrad and Kamm, 2006; Ouchi et al., 2003). The potential is given as

$$U_0(\{\mathbf{x_i}\}) = \sum_{i:\text{cell}} U_{\text{ar}}(A_i) + \sum_{[ij]:\text{edge}} U_{\text{lin}}^{ij}(l_{ij}) + \sum_{i:\text{cell}} U_{\text{cor}}(L_i) \tag{15}$$

where A_i and L_i represent the area and peripheral length of the ith cell at the plane of the adherens junction, respectively. l_{ij} is the length of the contact surface between the ith and jth cells. A_i, L_i, and l_{ij} are determined by positions of the vertices $\{\mathbf{x}_i\}$ which define the geometry of cells. The first term of Eq. (15) represents the area elasticity of a cell and is given by $U_{\text{ar}}(A)=(K/2)(A-A_0)^2$. The second term $U_{\text{lin}}^{ij}(l_{ij})=\sigma_{ij}l_{ij}$ represents cell adhesion and the contracting force, and the third term $U_{\text{cor}}(L)=(\Lambda/2)L^2$ represents cortical elasticity. Here coefficients of the second term, σ_{ij}, is randomly chosen from a Gaussian distribution with positive mean σ_0 and deviation Σ^2 (i.e., $P(\sigma) \propto \exp[-(\sigma-\sigma_0)^2/2\Sigma^2]$). We conducted the simulation until we obtained a stable configuration of cells. We calculated the "true values" of the cell pressures and edge tensions, $\mathbf{p}_{\text{true}}$, as $P_i= -K(A_i-A_0)$ and $T_{ij}=\sigma_{ij}+\Lambda(L_i+L_j)$, respectively. We then applied the estimation method for the configuration of cells and obtained $\mathbf{p}$, the "estimated values" of the cell pressures and edge tensions. Lastly, the estimated forces $\mathbf{p}$ were plotted against the true forces $\mathbf{p}_{\text{true}}$ after subtraction of the hydrostatic component and proper rescaling (Fig. 2B–D). For these data, the true and estimated values agreed with each other within about $\pm 5\%$ accuracy (correlation coefficients are 0.91 for tension and 0.98 for pressure in Fig. 2D).

We next confirmed the appropriateness of the obtained μ as follows. We searched for the weight μ' that minimized the $L2$ distance between $\mathbf{p}$ and $\mathbf{p}_{\text{true}}$, $||\mathbf{p}-\mathbf{p}_{\text{true}}||$. The obtained $\mathbf{p}$ could be regarded as the fittest estimation for the model. We then compared the results of the fittest and the maximum marginal likelihood estimations. The agreement between the two (Fig. 2G) indicated that the Bayesian determination of μ worked well.

We also tested alternative choices of priors (i.e., replace the second regularization terms in Eq. (7)). One possible regularization term is the $L2$ norm, which is often adopted to avoid over-fitting and is represented as $R_{L2}=\mu_1\Sigma_i\|P_i\|^2+\mu_2\Sigma_{[ij]} \|T_{ij}\|^2$. Another choice is to expect spatial smoothness, i.e., neighboring cells and connected contact surfaces tend to have similar values of pressures and tensions, respectively. A regularization term for smoothness is given by $R_{sm}=\mu_1\Sigma_i (P_i-P_j)^2+\mu_2\Sigma_{[ij],[kl]} (T_{ij}-T_{kl})^2$, where summation of the first term is conducted over all neighboring pairs of cells, and that of
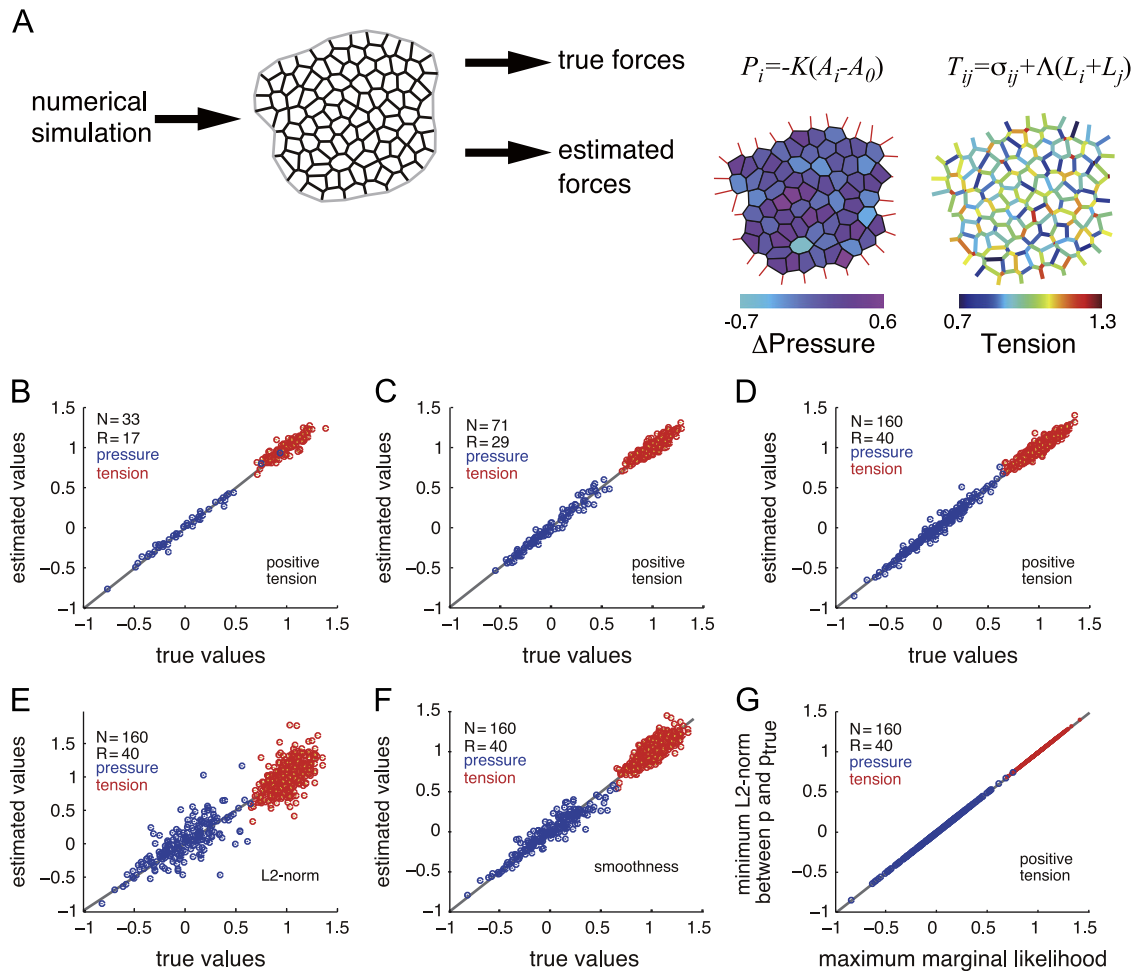
Fig. 2. *In silico* validation of the force-estimation method. (A) Flow chart for testing the estimation method using an artificially generated data set. (1) A numerical simulation of relaxing the potential was performed to generate cell configurations. Here, the "true forces" were determined by $P_i = -K(A_i - A_0)$ and $T_{ij} = \sigma_{ij} + \Lambda(L_i + L_j)$, where A_i and L_i are the area and peripheral length of the ith cell on the plane of the adherens junction, respectively. (2) The estimation procedure was applied to the cell configuration data. We then compared the true and estimated values. (B)–(F) Estimated relative pressures (blue) and tensions (red) are plotted against their true values. $N + R = 50$, 100, and 200 in (B)–(F), respectively. Results were obtained using regularization terms that represent (B)–(D) positive tension, (E) $L2$-norm (R_{L2}), and (F) spatial smoothness (R_{sm}). The regularization term that respects positive tension yielded the most accurate estimates among the regularization terms tested. (G) Results of the estimation obtained by minimizing $||\mathbf{p} - \mathbf{p}_{true}||$ for the same data as in D (the fittest estimation). The fittest and maximum marginal likelihood estimations were in agreement, indicating that the Bayesian determination of μ worked well. (For interpretation of the references to color in this figure legend, the reader is referred to the web version of this article.)

the second term is conducted over all connected pairs of contact surfaces. Estimating pressures and tensions for the artificial data by adjusting (μ_1, μ_2) to minimize $||\mathbf{p} - \mathbf{p}_{true}||$, we found that the estimation using R_{L2} or R_{sm} was not as accurate as that using the regularization term representing positive tension (Fig. 2E and F). Collectively, the prior distribution that respects positive tension is a reasonable choice for estimating the distribution of forces in a cell population.

2.3. In vivo validation of estimates of forces

To examine the validity of our method *in vivo*, we compared the estimated values with other readouts of forces such as responses to laser-induced destruction of cortical actin cables. The tension of an edge was estimated from image data just before laser irradiation (Fig. 3A left) and the maximum velocity of vertices of the ablated edge (V_{max}) was measured (Fig. 3A right). The estimates of the tension were in agreement with results obtained using a laser cutting method in both the *Drosophila* pupal wing and wing disc (Fig. 3B and C): edges with stronger and weaker tension exhibited larger and smaller V_{max}, respectively. We also checked that the estimated value of the tension was

correlated with the Myosin regulatory light chain (MRLC)-GFP signal (Royou et al., 2004) (Fig. 3D). Moreover, the estimated pressure indicated that the smaller the cell, the stronger the cell pressure (Fig. 4), which is consistent with the elastic nature of a cell and the photoelasticity measurements of the wing disc (Nienhaus et al., 2009). Furthermore, the anisotropy of the global stress in the pupal scutum and wing, which will be described in Section 2.5, was confirmed by ablating a group of cells (Sugimura et al., in preparation). These results strongly suggest that our method provides a reasonable estimate of forces *in vivo*.

2.4. Robustness against image processing error and deleting edges

To evaluate how image processing errors can affect the force-estimation, noise was added to all extracted positions of vertices. The noise applied had a Gaussian distribution, with a standard deviation of 1 pixel. Then, we estimated tensions and pressures using the noise data, and the standard deviation of the estimated values was calculated for 100 trials. For the sample of the *Drosophila* pupal wing shown in Fig. 5F, the standard deviation of the estimated pressure was only 0.0013, which is much smaller than that of the estimated dispersion of individual cell pressures.
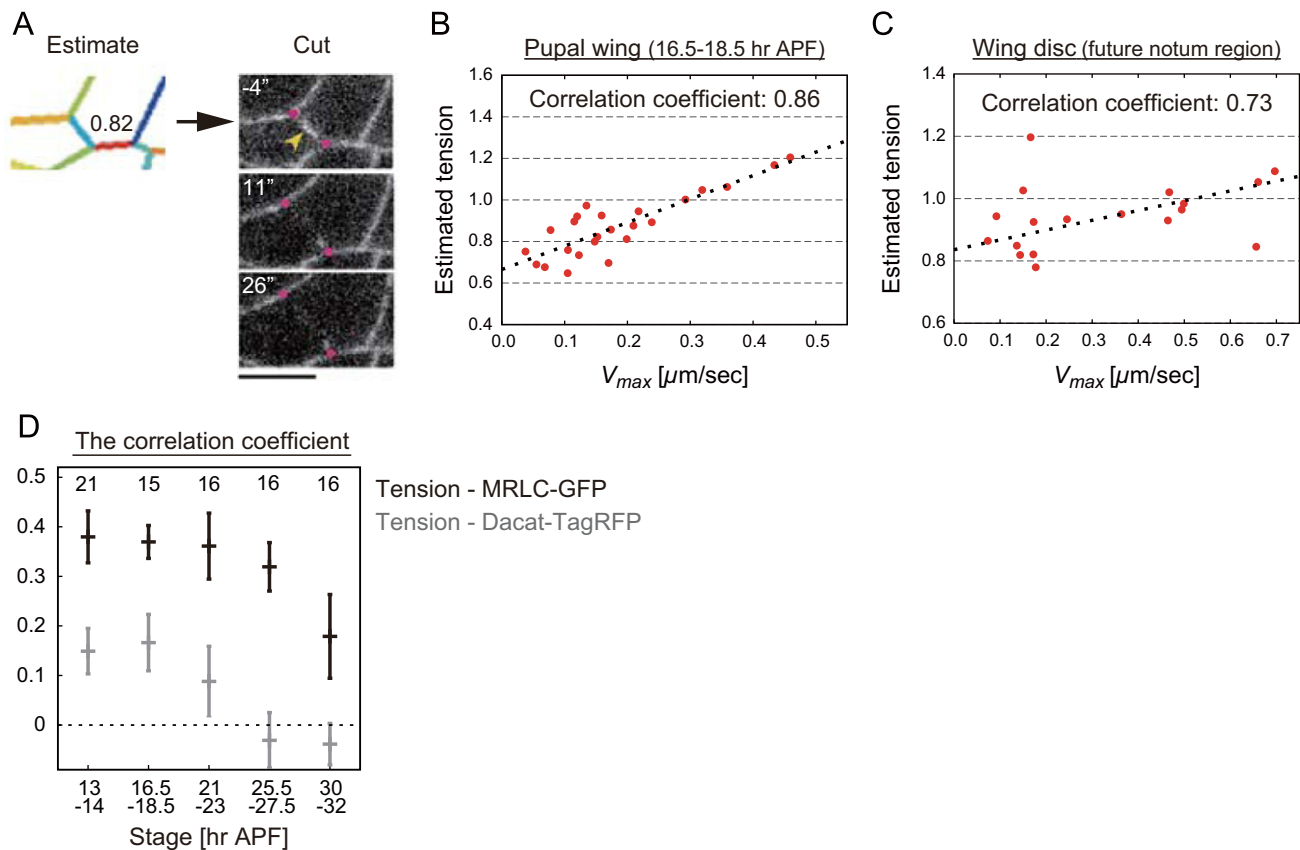
Fig. 3. *In vivo* validation of estimates of tensions. (A) The *Drosophila* pupal wing at 18 h 20 min APF. Left: the tension of an edge is estimated from image data just before cutting the edge. Right: a laser irradiates the edge (arrowhead) and the vertices of the manipulated edge are tracked (circles). (B) and (C) The estimated tension plotted against V_{max} of the vertices. One ablation per each pupal wing (B) or wing disc (C) was performed, and the average values of the estimated tension were normalized to 1. In (C), the correlation coefficients are calculated from all of the samples. For fitting data with a linear function (a dotted line), two obvious outliers are excluded. (D) The correlation coefficients between the estimated tension and signal intensity of MRLC-GFP (black) and Dαcatenin-TagRFP (grey) in the *Drosophila* pupal wing. The number of samples examined is indicated. The tension-myosin correlation was lower at 30–32 h APF when the biases in tension and myosin weakened. Scale bar: 5 μm (A).

The standard error of the estimated tension was also small (0.017 ± 0.007) and was less than 2% of the estimated tension. We obtained similar values for other samples. These results suggest that our force-estimation procedure is sufficiently robust to image processing errors.

We also checked the robustness of our force-estimation by randomly deleting $\sim$1% of edges (8 out of 838 edges) from the image in Fig. 5F. The standard deviation of the maximum stress direction was only 6.6×10^{-3} [rad] ($N=10$ samples). We also evaluated the anisotropy of the global stress, which is defined by the difference of two eigenvalues of the stress tensor given by Eq. (14). The standard deviation of the quantity was less than 1.5% of the value of the original data. Collectively, local error in an input image did not strongly affect our estimation of the global stress.

2.5. The distinctive patterns of forces in the Drosophila pupal scutum and wing

We applied our mechanical force inference method to the *Drosophila* pupal scutum (the anterior part of the dorsal thorax) and wing to characterize the stress field of these tissues (Fig. 5). Our analysis clarified that the scutum cells exhibited a moderately stronger tension on the anterior–posterior (AP) edges than on the lateral–medial (LM) edges at 23 h APF (after puparium formation) (Figs. 5E1 and 6C1; compare blue and red points in Fig. 6C2). On the other hand, in the wing, the estimated tensions were stronger in the proximal–distal (PD) edges than in the AP edges at the same developmental stage (arrows in Fig. 5F1). The directional bias in the estimated tension is larger in the wing than in the scutum at 23 h APF (compare Fig. 5E1 and F1; the comprehensive statistical analysis is published elsewhere), which is consistent with the larger anisotropy in local cell stress in the former (Fig. 5E3 and F3). In both tissues, the pressure was larger in smaller cells (Fig. 5E2 and F2; see also Fig. 4). By integrating the estimated tensions and pressures, we found that the global stress points to the AP axis and the PD axis in the scutum and wing, respectively (the long axis of the ellipse in Fig. 5E4 and F4). Therefore, the distinctive patterns of forces could be identified by our method.

Finally we analyzed developmental changes in the patterns of tensile force in the scutum (Figs. 6,7). As described above, the AP edges were estimated to have a stronger tension than the LM edges (Fig. 6A1–E1; compare blue and red points in Fig. 6A2–E2). The bias in tension was confirmed by laser cutting conducted at 19–21 h APF (Fig. 6F). We also evaluated the distribution of myosin regulatory light chain (MRLC). By 18.5 h APF, the MRLC–GFP signal was brighter in the AP than in the LM edges (Fig. 7A1–B3; compare arrowheads in Fig. 7B1 and B2), after which it became nearly uniform (Fig. 7C1–E3). Therefore, the estimated tension, response to laser cutting, and myosin distribution all indicated a moderately stronger tensile force on the AP edges. The maximum stress pointed in the AP direction throughout the developmental stages examined (the long axis of the ellipse in Fig. 6A2–E2) and cells were elongated along the AP axis (blue lines in Fig. 7B3–E3). These results were consistent with stretching of the scutum along the AP axis.
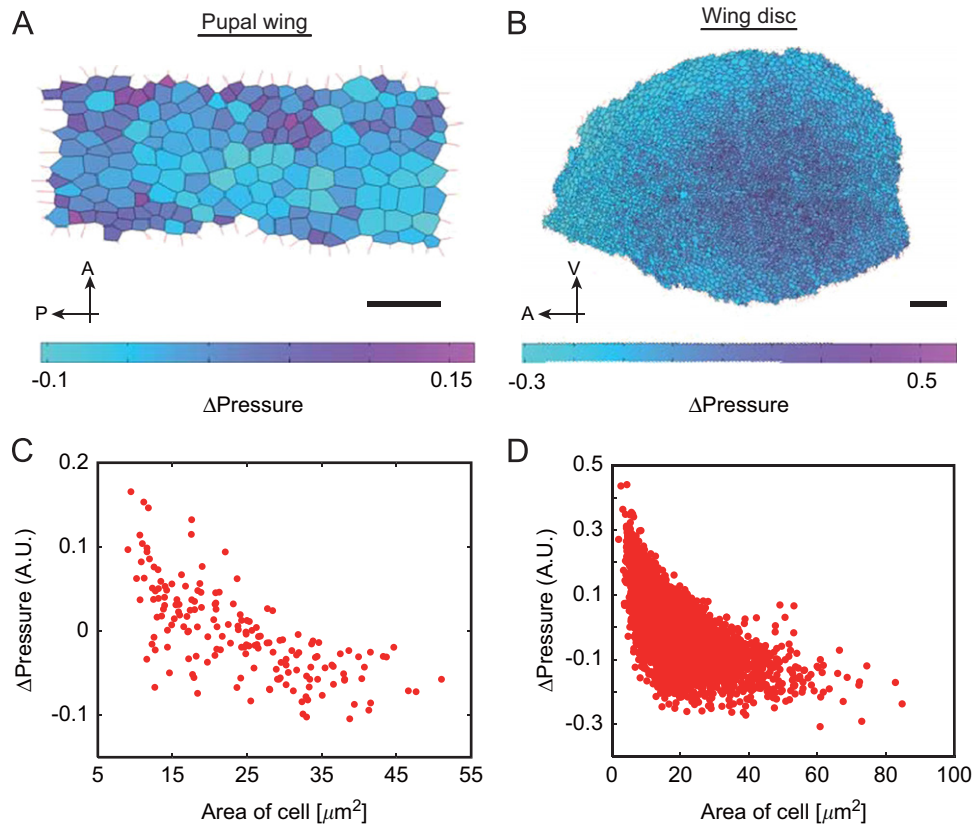
Fig. 4. The analysis of the patterns of the estimated pressures. (A)–(D) The pupal wings at 17 h 45 min APF (A) and (C) and the wing pouch of the wing discs (B)(D). (A) and (B) Patterns of the estimated pressures. In (B), cells in a central region have a stronger pressure than the cells in a peripheral region. This is consistent with results of a photoelasticity measurement of the disc, which indicates that the central region is more compressed than the peripheral region (Nienhaus et al., 2009). (C) and (D). The estimated pressure plotted against the area of the cell. They are negatively correlated. Scale bars: 20 μm (A) and (B).

3. Discussion

3.1. The advantages of our force-estimation method

The present study proposes a new inverse problem framework to quantify the distribution of forces in a developing tissue. The simplicity of the framework will allow its immediate application to other model systems, thereby shedding light on the mechanical control of a variety of morphogenetic processes. As the first step in this research direction, our quantification of spatio-temporal changes in the stress field and of the corresponding rearrangements of cells revealed that the balance of extrinsic and intrinsic forces regulates the packing of cells into a honeycomb pattern (Sugimura et al., in preparation). The advantages of our force-estimation method can be summarized as follows. First, the forces acting on more than 1000 cells can be estimated simultaneously at a single-cell resolution, which enables us to compare the estimated forces directly with the activity of the molecules responsible for generating the forces in each cell, as conducted for tension and myosin in this study. Second, it is noninvasive, and therefore one can analyze the spatiotemporal dynamics of a stress field. Third, no presumptive potential energy form is required (Eq. (15) was used only for a test of the method). As the validity of the forms of potential energy has not yet been fully evaluated, this feature is of critical importance. We believe that combining our method with those that measure the fast dynamics of force-generating molecules (Rauzi et al., 2010) and macroscopic mechanical features of a tissue (Bonnet et al., 2012; Moore et al., 1995; Nienhaus et al., 2009; Savin et al., 2011) will contribute a fruitful new research direction.

3.2. Dynamic analysis

Under an assumption of quasi-static cell shape changes, we can estimate the cell pressure and the cortical tension from a still image of cells. This feature of our method is in a sharp contrast with a mechanical inference method (Brodland et al., 2010), which was reported just before the first submission of the manuscript on this work. Nevertheless, it would be worth considering a way to incorporate temporal dynamics of cell shape changes/forces in our estimation framework. The force balance equation with drag force is given by $\mathbf{Ap} = \mathbf{\Gamma v}$, where $\mathbf{v}$ is a vector composed of the velocities of vertices, $d\mathbf{x}_i/dt$, and $\mathbf{\Gamma}$ is an $n \times n$ positive definite matrix that represents generalized drag coefficients. Our Bayesian formulation can be applied immediately to the adapted inverse problem by substituting $\mathbf{\Gamma v}$ for $\mathbf{b}$ in Eq. (5). The correct form of $\mathbf{\Gamma}$ in an epithelial tissue is so far unknown. The simple form $\Gamma_{ii} = \gamma \delta_{ij} \, (\gamma > 0)$ is often employed (Eiraku et al., 2011; Rauzi et al., 2008), whereas another that considers the relative velocity in the local area (local strain rate) should be tested (Brodland et al., 2010). In addition, the following technical points should be noted. (i) The time interval between consecutive time points must be appropriately tuned. A too long time interval will lose temporal information of cell shape changes, whereas we noticed that a too short time interval also leads to an inaccurate evaluation of the velocity due to the increased susceptibility to image processing error. (ii) The neighbor exchange (T1 process) should be appropriately treated. For instance, one might consider interpolating the position of the vertices and timing of the neighbor exchange. (iii) The accurate detection and tracking of hundreds to thousands of cells in more than 100 sequential images require a very sophisticated algorithm (Aigouy et al.,
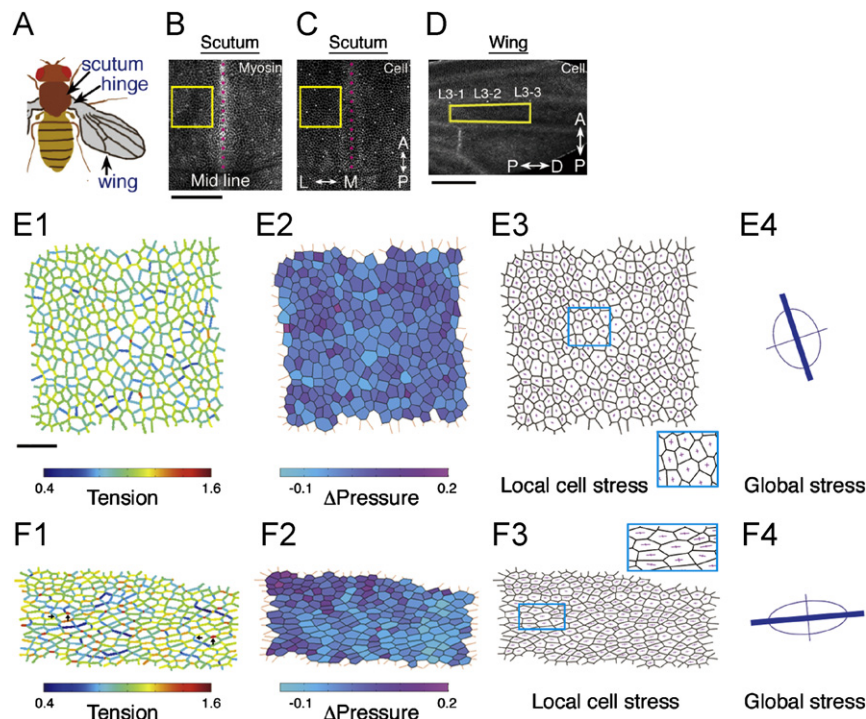
Fig. 5. The patterns of tension in the *Drosophila* scutum and wing. (A) Schematic of an adult *Drosophila*. (B) and (C) A wide image of the *Drosophila* pupal scutum (the anterior part of the dorsal thorax) expressing MRLC-GFP under the control of a promoter of the *MRLC* gene (B) and a cell shape marker (Dαcatenin-TagRFP) (C) at 24.5 h APF. As spatial landmarks, we used the midline of the body (dotted line), where a very strong signal for MRLC-GFP was observed at the deep *z*-planes. We analyzed a region adjacent to the midline (square). In all images of the pupal scutum, anterior is up and lateral is left. We set the midline as the AP axis. (D) A wide image of the wing at 32 h APF. As spatial landmarks, we used three sensory organs on the L3 vein (L3–1 to L3–3) and analyzed the inter-vein region between L3–1 and L3–3 (rectangle). In all images of the pupal wing, the vertical and horizontal directions are aligned with the anterior–posterior (AP) and proximal–distal (PD) axes, respectively. We set a line connecting L3-1 and L3-3 as the PD axis. (E1)–(E4) The scutum at 23 h APF. (F1)–(F4) The wing at 23 h APF. The estimated tension (E1) and (F1), relative pressure (E2) and (F2), local cell stress (E3) and (F3) and global stress (E4) and (F4) are shown. In F1, arrows point to the PD and AP edges. In E3 and F3, a cross indicates the longest and shortest axes of the stress ellipse of each cell. Note that the aspect ratio of the local and global stress ellipse is larger in the wing than in the scutum (insets in E3 and F3; E4 and F4). Scale bars: 100 μm (B) and (D) and 20 μm (E1) and (F1).
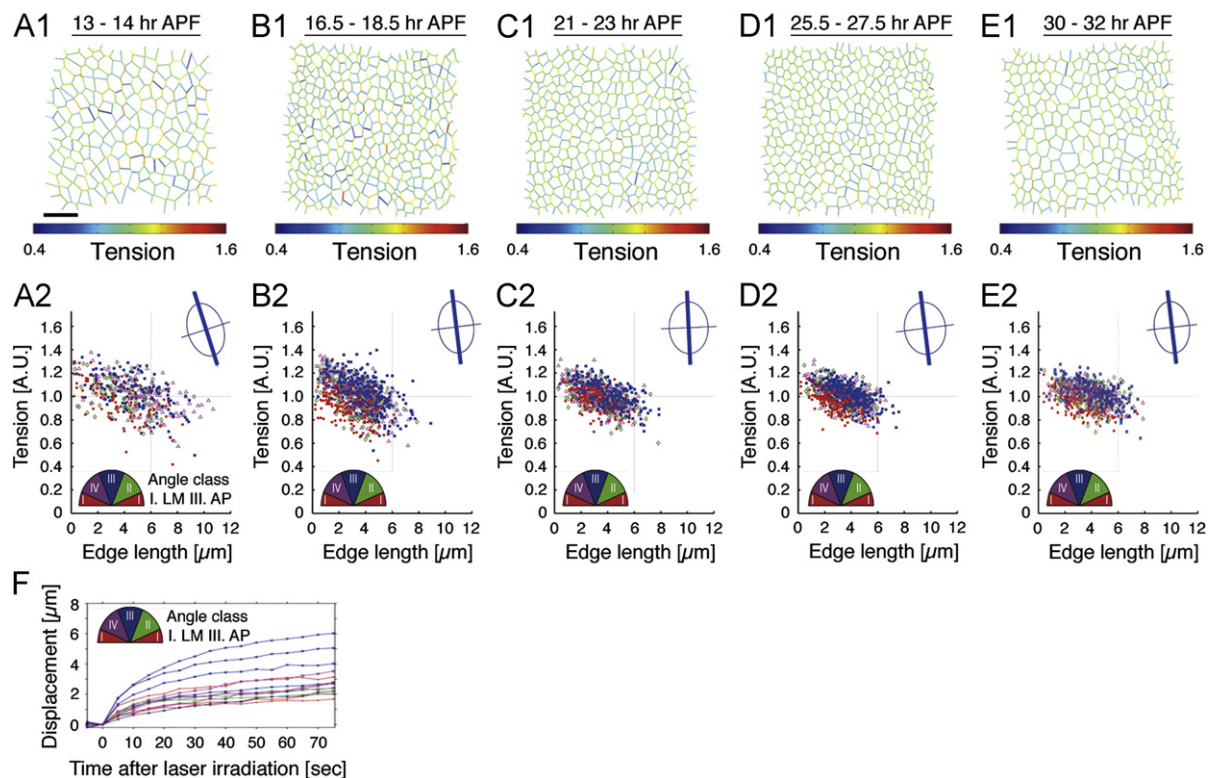

Fig. 6. Developmental changes in the patterns of tension in the scutum. (A1)–(E1) Patterns of estimated tension at the stages indicated. (A2)–(E2) The direction of each edge is classified (e.g., red class I for the LM edges and blue class III for the AP edges) and its estimated tension plotted against its length. The longest axis of the ellipse represents the maximum stress direction of a group of cells. (F) Time evolution of the displacement of the vertices after the laser-induced destruction of the cortical actin network at 19–21 h APF. Scale bar: 20 μm (A1). (For interpretation of the references to color in this figure legend, the reader is referred to the web version of this article.)
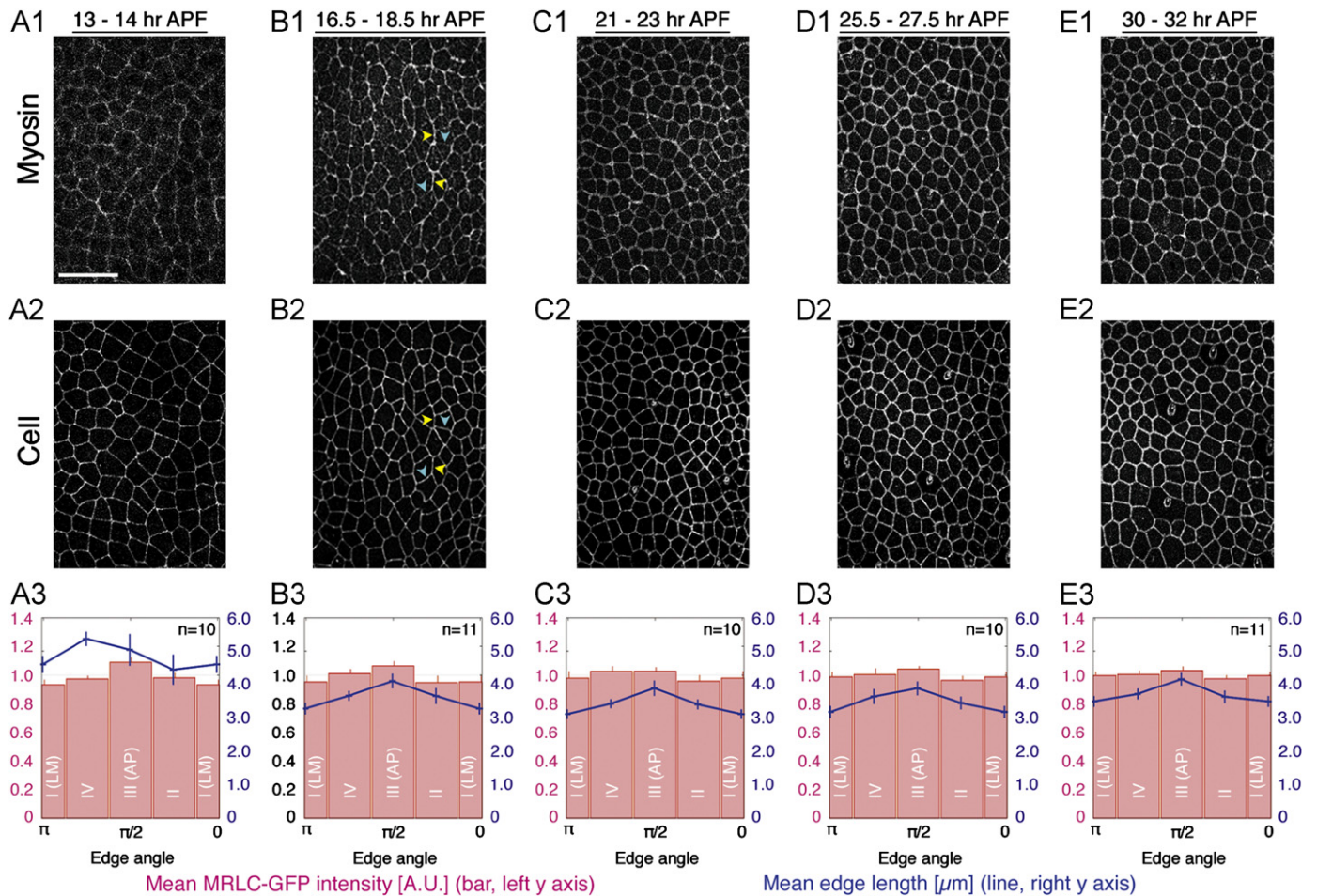
Fig. 7. Developmental changes in the distribution of the myosin subunit in the scutum. (A1)–(E2) Images of the scutum expressing MRLC-GFP under the control of a promoter of the *MRLC* gene (A1)–(E1) and a cell shape marker (Dαcatenin-TagRFP) (A2)–(E2) at the stages indicated. In (A2) and (B2), The yellow and blue arrowheads indicate the AP and LM edges, respectively. (A3)–(E3) Quantification of the mean signal intensity of MRLC-GFP (bar, left *y*-axis) and the average length of the edges (line, right *y*-axis) for each angle class. Scale bar: 20 µm (A1). (For interpretation of the references to color in this figure legend, the reader is referred to the web version of this article.).

2011; Bosveld et al., 2012). Therefore, a substantial number of studies will be required to incorporate temporal information into our force-estimation framework.

3.3. Inverse problem based on Bayesian statistics

In an inverse problem, the number of the conditions is often less than that of unknowns (Kaipio and Somersalo, 2004). By considering the expected features of the system, one can choose the most plausible solution. Classically, inverse problems were formulated as minimizing the sum of squares error (fit-of-data) and regularization (expectation) terms. However, classical methods do not have a criterion for determining the weight parameter for the latter. Bayesian statistics has been proven to provide a more fundamental formalism for inverse problems, in which information criteria, such as the Akaike Bayesian information criterion (ABIC), determine the weight of regularization term(s). Nowadays, Bayesian frameworks of inverse problem are widely applied to various phenomena (computer vision, seismology, electroencephalograms, etc.) (Kaipio and Somersalo, 2004).

The present study handles the inherent indefiniteness in the force-estimation in an epithelial sheet by formulating the inverse problem based on Bayesian statistics. A clear theoretical interpretation of the estimation process and the plausible balance between fit-of-data and expectation of the system represent the advantages of our method over other force-estimation methods

(Brodland et al., 2010; Chiou et al., 2012), where indefiniteness in the force-balance equations was treated by arbitrary assumptions such as zero-tension edges or uniform pressures. More importantly, the Bayesian statistics-based formulation provides criteria for model selection that enable us to extend our model on the consistent theoretical ground of modern statistical theory. More complex models with more fitting parameters, of course, fit the data better (higher likelihood). However, with criteria such as ABIC, in the future we can reasonably extend our model by compromising between the model complexity and the quality of the obtained data.

3.4. Conclusion

Morphogenesis proceeds at multiple scales spanning a range from molecular reactions to tissue/body deformation. The described force-estimation technique, which can quantify forces and stresses at cellular and cell-population scales, provides a powerful tool for dissecting such hierarchical dynamics.

Acknowledgements

Appendices

A.1. Image collection

The genotypes of flies used were *sqhp-sqhGFP*, *apterous-gal4/sqhp-sqhGFP*, *UAS-Dαcatenin-TagRFP* (Figs. 1B, 3A, B and D, 4A and C, 5, 6, 7) and *ubp-DEcadherin-GFP* (Oda and Tsukita, 2001) (Figs. 3C, 4B and D). Preparation of samples of the *Drosophila* pupal wing and scutum for image collection was conducted as previously described (Koto et al., 2009; Shimada et al., 2006). Images were acquired using an inverted confocal microscope (FV1000D; Olympus) equipped with an Olympus 60x/NA1.2 SPlanApo water-immersion objective at 25 °C unless otherwise noted.

A.2. Construction of UAS-Dαcatenin-TagRFP line

To highlight the shape of the cell at the level of the adherens junction, *TagRFP* was cloned into NcoI-XbaI-cut pBS-DCT-GFP to fuse it to the C-terminal of the *Dαcatenin* coding sequence (*EGFP* was replaced by TagRFP) (Oda and Tsukita, 1999). *Dαcatenin-TagRFP* was then inserted into KpnI-XbaI-cut pUAST and transgenic flies were produced.

A.3. Laser ablation experiment

The pupae and wing disc were mounted in a chamber as previously described (Farhadifar et al., 2007; Koto et al., 2009). A 2-photon laser tuned to the 720 nm wavelength (MaiTai HP-DeepSee-OL; Spectra-Physics) irradiated a very small region of the cell cortex in point-scan mode (0.041 μm/pixel). The duration of the stimulus was 5 ms with an approximate power of 75 mW (pupa) and 45 mW (disc) at the surface of the objective lens. In parallel with the ablation, images were acquired at 5 s intervals on an upright confocal microscope (FV1000D; Olympus).

A.4. Image processing and analysis

We extracted cells using a custom-made macro and plug-ins in ImageJ. We checked all of the skeletonized patterns and manually modified them, if necessary. While counting the number of edges for each cell, we calculated the distance between the centers of the end pixels of an edge. If the distance was smaller than 3 pixels in length, the edge was regarded as a four-way vertex. As for dividing cells in telophase, the constriction ring, which is indicated by the intracellular distribution of myosin, is regarded as an edge.

To quantify the MRLC-GFP (Royou et al., 2004) signal intensity at the edges for an image captured at several *z*-planes, the following procedures were applied. First, we extracted the MRLC signals on the same plane as the Dαcatenin signals. Next, the mean signal intensity of each plane was normalized to eliminate the effect of weakening signal intensities at deeper *z*-planes. In addition, to avoid a signal at a vertex being counted for all the edges connected to it, we omitted the signals for 2 pixels at the ends of the edges when calculating the mean signal intensity along each edge (thus, we excluded edges shorter than 4 pixels in length). We confirmed that the values of the eliminated pixels did not affect the results. Image processing and analysis were done with ImageJ, MATLAB, and OpenCV. The images were processed using 'subtract background' command in ImageJ. We found that in each of the four angular classes, the value of the correlation coefficient between myosin signal intensity and tension did not decrease when quantified. Therefore, it was thought that this correlation did not simply result from the angular dependencies of myosin and tension. To examine the statistical significance of the correlation between myosin and tension in detail, we calculated the correlation in permuted edges. After permuting the edges, the mean and standard deviation value of the correlation coefficient greatly decreased (0.00017 and 0.04538, respectively for the wing shown in Fig. 5F). Similar values were obtained in all other samples.

References

Aigouy, B., Farhadifar, R., Staple, D.B., Sagner, A., Roper, J.C., Julicher, F., Eaton, S., 2011. Cell flow reorients the axis of planar polarity in the wing epithelium of *Drosophila*. Cell 142, 773–786.

Akaike, H., 1980. Likelihood and the Bayes procedure. In: Bernardo, J.M., DeGroot, M.H., Lindley, D.V., Smith, A.F.M. (Eds.), In Bayesian statistics. Valencia, University Press.

Batchelor, G.K., 1970. The stress system in a suspension of force-free particles. J. Fluid Mech. 41, 545–570.

Bilder, D., Haigo, S.L., 2012. Expanding the morphogenetic repertoire: perspectives from the *Drosophila* egg. Dev. Cell 22, 12–23.

Bonnet, I., Marcq, P., Bosveld, F., Fetler, L., Bellaiche, Y., Graner, F., 2012. Mechanical state, material properties and continuous description of an epithelial tissue. J R Soc Interface.

Bosveld, F., Bonnet, I., Guirao, B., Tlili, S., Wang, Z., Petitalot, A., Marchand, R., Bardet, P.L., Marcq, P., Graner, F., et al., 2012. Mechanical control of morphogenesis by Fat/Dachsous/Four-jointed planar cell polarity pathway. Science 336, 724–727.

Brodland, G.W., Conte, V., Cranston, P.G., Veldhuis, J., Narasimhan, S., Hutson, M.S., Jacinto, A., Ulrich, F., Baum, B., Miodownik, M., 2010. Video force microscopy reveals the mechanics of ventral furrow invagination in *Drosophila*. Proc. Nat. Acad. Sci. U.S.A. 107, 22111–22116.

Chiou, K.K., Hufnagel, L., Shraiman, B.I., 2012. Mechanical stress inference for two dimensional cell arrays. PLoS Comput. Biol. 8, e1002512.

Demmel, J.W., 1997. Applied Numerical Algebra. Society for Industrial and Applied Mathematics, Philadelphia, PA 1997.

Eaton, S., Julicher, F., 2012. Cell flow and tissue polarity patterns. Curr. Opin. Genet. Dev. 21, 747–752.

Eiraku, M., Takata, N., Ishibashi, H., Kawada, M., Sakakura, E., Okuda, S., Sekiguchi, K., Adachi, T., Sasai, Y., 2011. Self-organizing optic-cup morphogenesis in three-dimensional culture. Nature 472, 51–56.

Farhadifar, R., Roper, J.C., Aigouy, B., Eaton, S., Julicher, F., 2007. The influence of cell mechanics, cell-cell interactions, and proliferation on epithelial packing. Curr. Biol. 17, 2095–2104.

Henle, M.A. (1994). Combinatorial Introduction to Topology (New York, Dover).

Honda, H., 1983. Geometrical Models for Cells in Tissues. Int. Rev. Cytol. -A Surv. Cell Biol. 81, 191–248.

Hutson, M.S., Tokutake, Y., Chang, M.S., Bloor, J.W., Venakides, S., Kiehart, D.P., Edwards, G.S., 2003. Forces for morphogenesis investigated with laser microsurgery and quantitative modeling. Science 300, 145–149.

Käfer, J., Hayashi, T., Maree, A.F., Carthew, R.W., Graner, F., 2007. Cell adhesion and cortex contractility determine cell patterning in the *Drosophila* retina. Proc. Nat. Acad. Sci. U.S.A. 104, 18549–18554.

Kaipio, J., Somersalo, E., 2004. Statistical and Computational Inverse Problems. Springer, New York.

Kasza, K.E., Zallen, J.A., 2011. Dynamics and regulation of contractile actin-myosin networks in morphogenesis. Curr .Opin. Cell Biol. 23, 30–38.

Koto, A., Kuranaga, E., Miura, M., 2009. Temporal regulation of *Drosophila* IAP1 determines caspase functions in sensory organ development. J. Cell Biol. 187, 219–231.

Lecuit, T., Lenne, P.F., 2007. Cell surface mechanics and the control of cell shape, tissue patterns and morphogenesis. Nat. Rev. Mol. Cell Biol. 8, 633–644.

Lecuit, T., Lenne, P.F., Munro, E., 2011. Force generation, transmission, and integration during cell and tissue morphogenesis. Annu. Rev. Cell Dev. Biol. 27, 157–184.

Mason, F.M., Martin, A.C., 2011. Tuning cell shape change with contractile ratchets. Curr. Opin. Genet. Dev. 21, 671–679.

Mofrad, M.R.K., Kamm, R.D., 2006. Cytoskeletal Mechanics. Cambridge University Press, Cambridge.

Moore, S.W., Keller, R.E., Koehl, M.A., 1995. The dorsal involuting marginal zone stiffens anisotropically during its convergent extension in the gastrula of Xenopus laevis. Development 121, 3131–3140.

Nahmad, M., Lander, A.D., 2011. Spatiotemporal mechanisms of morphogen gradient interpretation. Curr. Opin. Genet. Dev. 21, 726–731.

Nienhaus, U., Aegerter-Wilmsen, T., Aegerter, C.M., 2009. Determination of mechanical stress distribution in Drosophila wing discs using photoelasticity. Mech. Dev. 126, 942–949.

Oda, H., Tsukita, S., 1999. Dynamic features of adherens junctions during Drosophila embryonic epithelial morphogenesis revealed by a Dalpha-catenin-GFP fusion protein. Dev. Genes Evol. 209, 218–225.

Oda, H., Tsukita, S., 2001. Real-time imaging of cell--cell adherens junctions reveals that Drosophila mesoderm invagination begins with two phases of apical constriction of cells. J. Cell Sci. 114, 493–501.

Ouchi, N.B., Glazier, J.A., Rieu, J.P., Upadhyaya, A., Sawada, Y., 2003. Improving the realism of the cellular Potts model in simulations of biological cells. Phys. A-Stat. Mech. Its Appl. 329, 451–458.

Paluch, E., Heisenberg, C.P., 2009. Biology and physics of cell shape changes in development. Curr. Biol. 19, R790–R799.

Raffel, M., Willert, C., Kompenhans, J., 1998. Particle Image Velocimetry: A Practical Guide. Springer, Berlin.

Rauzi, M., Lenne, P.F., Lecuit, T., 2010. Planar polarized actomyosin contractile flows control epithelial junction remodelling. Nature 468, 1110–1114.

Rauzi, M., Verant, P., Lecuit, T., Lenne, P.F., 2008. Nature and anisotropy of cortical forces orienting Drosophila tissue morphogenesis. Nat. Cell Biol. 10, 1401–1410.

Royou, A., Field, C., Sisson, J.C., Sullivan, W., Karess, R., 2004. Reassessing the role and dynamics of nonmuscle myosin II during furrow formation in early Drosophila embryos. Mol. Biol. Cell 15, 838–850.

Savin, T., Kurpios, N.A., Shyer, A.E., Florescu, P., Liang, H., Mahadevan, L., Tabin, C.J., 2011. On the growth and form of the gut. Nature 476, 57–62.

Shimada, Y., Yonemura, S., Ohkura, H., Strutt, D., Uemura, T., 2006. Polarized transport of Frizzled along the planar microtubule arrays in Drosophila wing epithelium. Dev. Cell 10, 209–222.

Supatto, W., Debarre, D., Moulia, B., Brouzes, E., Martin, J.L., Farge, E., Beaurepaire, E., 2005. In vivo modulation of morphogenetic movements in Drosophila embryos with femtosecond laser pulses. Proc. Nat. Acad. Sci. U.S.A. 102, 1047–1052.

Wartlick, O., Gonzalez-Gaitan, M., 2011. The missing link: implementation of morphogenetic growth control on the cellular and molecular level. Curr. Opin. Genet Dev. 21, 690–695.